electronics

MDPI

Article

Dual-Core Photonic Crystal Fiber Polarization Beam Splitter Based on a Nematic Liquid Crystal with an Ultra-Short Length and Ultra-Wide Bandwidth

Yuxiang Ji [1], Yuhang Du [2], Jixuan Dai [3], Hui Zou [1,*], Ruizhe Zhang [2] and Dinghao Zhou [1]

[1] College of Electronic and Optical Engineering & College of Flexible Electronics (Future Technology), Nanjing University of Posts and Telecommunications, Nanjing 210023, China
[2] Bell Honors School, Nanjing University of Posts and Telecommunications, Nanjing 210023, China
[3] Portland Institute, Nanjing University of Posts and Telecommunications, Nanjing 210023, China
* Correspondence: huizou@njupt.edu.cn

Abstract: This paper presents a novel pentagonal structure dual-core photonic crystal fiber polarizing beam splitter (PS-DC-PCF PBS) filled with a nematic liquid crystal (NLC) in the central hole. Unlike previous designs with symmetric arrangements, the upper and lower halves of the structure have different air hole arrangements. The upper half consists of air holes arranged in a regular quadrilateral pattern, while the lower half features a regular hexagonal arrangement of air holes. By filling the central hole with birefringent liquid crystal, the birefringence of the structure is enhanced, reducing the coupling lengths along the x polarization and y polarization directions. The polarization properties, coupling characteristics, and the influence of different structural parameters on the extinction ratio of the polarizing beam splitter are analyzed using the full-vector finite element method. Simulation results demonstrate that the designed PS-DC-PCF PBS achieves a maximum extinction ratio (ER) of 72.94 dB with a splitting length of only 61.9 μm and a wide operating bandwidth of 423 nm (1.324–1.747 μm), covering most of the O, E, S, C, L, and U communication bands. It exhibits not only ultra-short splitting lengths and ultra-wide splitting bandwidth but also good manufacturing tolerances and anti-interference capabilities. The designed PS-DC-PCF PBS could provide crucial device support for future all-optical communication systems and has potential applications in fiber optic communication or fiber laser systems.

Keywords: PS-DC-PCF PBS; NLC; ultra-short splitting lengths; ultra-wide splitting bandwidth

check for updates

Citation: Ji, Y.; Du, Y.; Dai, J.; Zou, H.; Zhang, R.; Zhou, D. Dual-Core Photonic Crystal Fiber Polarization Beam Splitter Based on a Nematic Liquid Crystal with an Ultra-Short Length and Ultra-Wide Bandwidth. *Electronics* **2024**, *13*, 2343. https://doi.org/10.3390/electronics13122343

Academic Editor: Nakkeeran Kaliyaperumal

Received: 30 May 2024
Revised: 7 June 2024
Accepted: 13 June 2024
Published: 15 June 2024

Copyright: © 2024 by the authors. Licensee MDPI, Basel, Switzerland. This article is an open access article distributed under the terms and conditions of the Creative Commons Attribution (CC BY) license (https://creativecommons.org/licenses/by/4.0/).

1. Introduction

The polarization beam splitter (PBS) plays a crucial role in optical communication systems by effectively separating two different polarization modes within a light beam. However, with the rapid advancement of optical communication technology, traditional PBS based on conventional optical fibers has gradually become inadequate to meet practical demands, primarily due to limitations such as long splitting lengths and poor performance. Since 1996, photonic crystal fiber (PCF) has garnered significant attention due to its flexible tunable structure and unique optical characteristics [1], positioning it as a highly promising design solution for PBS [2–4].

So far, there have been numerous reports on PBS based on PCF. There are primarily two types of PBS based on PCF, including dual-core PCF (DC-PCF) PBS [5–7] and triple-core PCF (TC-PCF) PBS [8–10]. However, due to the more challenging manufacturing process of TC-PCF, some research efforts have focused on DC-PCF PBS. In previous works, better polarization and coupling characteristics for PCF PBS could be achieved by altering the arrangement of cladding air holes or by filling certain air holes with functional materials. This resulted in improved performance of the PBS based on PCF.

Currently, research on liquid crystal-enhanced PCF PBS has gained significant attention. In 2018, Younis B. M. et al. introduced an asymmetric DC-PCF (ADC-PCF) wavelength-selective PBS with a splitting length of 5.678 mm, exhibiting an extremely narrow bandwidth of about 3 nm around wavelengths of 1.3 μm and 1.55 μm [11]. However, despite the breakthrough achieved at that time, both the splitting length and operational bandwidth of this design have not yet reached an ideal state, leaving room for further improvement. Subsequently, in 2021, S. An et al. proposed a simple and efficient nematic liquid crystal-filled DC-PCF PBS [12], which made significant progress in both splitting length and operational bandwidth. The length of this design was only 13.3390 μm, with a maximum extinction ratio (ER) of 143.49 dB and a bandwidth of over 10 dB, reaching 200 nm. Although the bandwidth increased compared to the previous design, there is still room for optimization. In the same year, Yuwei Qu et al. introduced a novel liquid crystal-filled DC-PCF PBS (LC-DC-PCF PBS) [13], achieving a breakthrough in operational bandwidth and further reducing the splitting length. The final splitting length was only 94 μm, with a spectral bandwidth of 349 nm, covering the entire E + S + C + L + U communication band. In 2023, Yanan Xu et al. proposed an ultra-short polarization beam splitter based on a center-filled-hole DC-PCF (RS-DC-PCF) [14]. The ultra-short splitting length of this device was 58 μm, with an ER greater than 20 dB over a wavelength range of 1.306 to 1.641 μm, and a bandwidth of 335 nm, covering most of the O + E + S + C + L communication bands. Despite a slight decrease in operational bandwidth compared to previous studies, this design achieved a shorter splitting length. In summary, these liquid crystal-based PCF PBS designs still have significant room for improvement and enhancement in terms of operational bandwidth and splitting length.

Therefore, in this paper, a pentagonal structure DC-PCF (PS-DC-PCF) PBS is proposed, which achieves a wider operational bandwidth than the aforementioned liquid crystal-based PCF PBS research results and has a shorter splitting length. In the design, the PS-DC-PCF structure includes five sizes of air holes arranged in a pentagonal lattice. The coupling length and coupling length ratio of the PS-DC-PCF PBS are calculated using the mode coupling theory and full-vector finite element method (FV-FEM). The effects of fabrication tolerances of the five air hole sizes as well as temperature and the nematic liquid crystal (NLC) molecular angle on the performance of the PS-DC-PCF PBS are analyzed. Finally, a well-performing ultra-short PS-DC-PCF PBS is obtained, with a splitting length of only 61.9 μm, a maximum ER of 72.94 dB, and a bandwidth of up to 423 nm, covering most of the communication bands in O + E + S + C + L + U. Compared with previous studies, it achieves a wider operational bandwidth while having a shorter splitting length.

2. Design of the PS-DC-PCF PBS and Theory

The cross-section of the designed PS-DC-PCF PBS is illustrated in Figure 1. From Figure 1, it can be observed that the proposed PS-DC-PCF PBS features a pentagonal overall air hole structure, with different arrangement patterns in the upper and lower sections. The upper half exhibits a quadrilateral arrangement of air holes, while the lower half presents a hexagonal arrangement. The central air hole, with a diameter of d_1, is filled with an NLC (E7). The NLC (E7), characterized by its anisotropy, significantly enhances the birefringence of the structure. The higher refractive index of the NLC (E7) ensures effective confinement of the optical field within the core region. Cores A and B are formed by selectively removing the left and right adjacent air holes to the central air hole, respectively. Surrounding the cores A and B, there are four types of air holes with different sizes: 9 small air holes adjacent to the core region in the y direction with a diameter of d_2, 5 small air holes above the core region, and 4 small air holes below the core region, thereby breaking the symmetry of the structure and achieving higher birefringence characteristics. In the x direction, the diameter of the two large air holes adjacent to cores A and B is d_3, while the diameters of the remaining air holes in the upper and lower halves of the cross-section are d_4 and d_5, respectively. The spacing between adjacent air holes in the y direction is denoted as Λ, while in the x direction, it is denoted as Λ for adjacent quadrilateral arranged air holes in

the upper half of the cross-section and $\sqrt{3}/3\Lambda$ for adjacent hexagonal arranged air holes in the lower half. The substrate material of the PS-DC-PCF PBS is silica dioxide. To reduce the transmission loss of optical energy in simulations using the FV-FEM, a Perfectly Matched Layer (PML) is added as the outermost layer of the structure. The thickness of the PML is set to Λ, with a refractive index 0.03 higher than that of the silica dioxide material [15]. The proposed PS-DC-PCF PBS was modelled and analyzed using COMSOL Multiphysics 5.6 software. PML and scattering boundary conditions were used to fix the computational region and to absorb internal radiation, and the mesh delineation of the NLC center holes and air holes was carefully optimized to make the calculations more accurate.

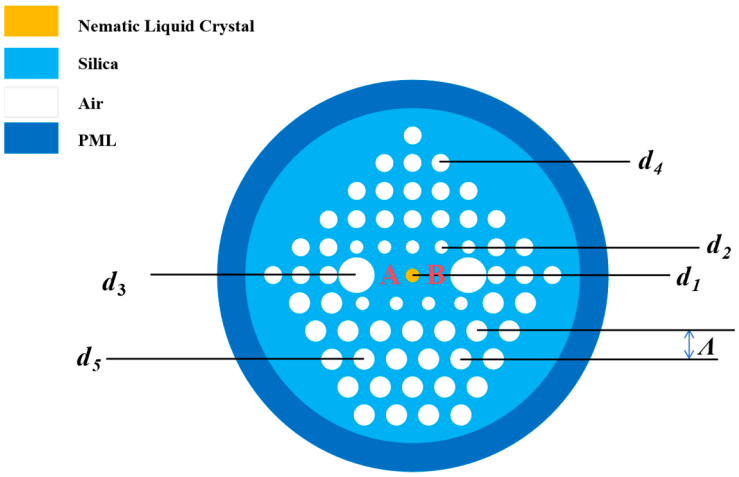

Figure 1. Cross-section of the designed PS-DC-PCF PBS with a central hole filled nematic liquid crystal.

The Sellmeier equation can be used to calculate the refractive index (n_{silica}) of silicon dioxide at different wavelengths [16–18].

$$n_{\text{silica}}(\lambda) = \sqrt{1 + \frac{A_1\lambda^2}{\lambda^2 - B_1^2} + \frac{A_2\lambda^2}{\lambda^2 - B_2^2} + \frac{A_3\lambda^2}{\lambda^2 - B_3^2}}, \tag{1}$$

where λ is the wavelength of the incident light in free space, A_1 = 0.6961663, A_2 = 0.407926, A_3 = 0.8974794, B_1 = 0.0684043 µm, B_2 = 0.1162414 µm, and B_3 = 9.896161 µm.

The refractive index of the NLC (E7) can be calculated using the Cauchy model [19,20], which includes the unusual refractive index no and the very refractive index ne. This refractive index is anisotropic over a range of temperatures.

$$n_0 = A_0 + \frac{B_0}{\lambda^2} + \frac{C_0}{\lambda^4}, \tag{2}$$

$$n_e = A_e + \frac{B_e}{\lambda^2} + \frac{C_e}{\lambda^4}, \tag{3}$$

The temperature dependent coefficients, A_o, B_o, C_o, A_e, B_e and C_e, are given in Table 1. The definition of the relative dielectric constant tensor ε_r of the NLC (E7) is as follows [21]:

$$\varepsilon_r = \begin{pmatrix} n_0^2 \sin^2\varphi + n_e^2 \cos^2\varphi & (n_e^2 - n_o^2)\cos\varphi\sin\varphi & 0 \\ (n_e^2 - n_o^2)\cos\varphi\sin\varphi & n_o^2\cos^2\varphi + n_e^2\sin^2\varphi & 0 \\ 0 & 0 & n_o^2 \end{pmatrix}, \tag{4}$$

Table 1. Detailed values of the refractive index coefficients of the NLC (E7) at different temperatures.

T (°C)	A_o	B_o (μm^2)	C_o (μm^4)	A_e	B_e (μm^2)	C_e (μm^4)
15	1.5006	0.0065	0.0004	1.7055	0.0087	0.0028
25	1.4994	0.0070	0.0004	1.6933	0.0078	0.0028
35	1.4987	0.0071	0.0004	1.6761	0.0091	0.0025
45	1.5062	0.0068	0.0006	1.6565	0.0083	0.0024

The inclination of the NLC molecule's long axis concerning the x-axis is denoted by φ, as illustrated in Figure 1, with a value range of [0, 90°]. The magnitude of φ is influenced by the external electric field, thereby allowing for controlled manipulation. For instance, positioning the proposed PS-DC-PCF PBS between two planar electrodes and adjusting the external electric field enables modification of the NLC (E7) molecule arrangement [22–24]. Specifically, when the long axis of the NLC (E7) molecule aligns parallel to the x-axis, φ equals 0 degrees, while an alignment parallel to the y-axis corresponds to φ being 90 degrees. This dynamic illustrates the tunable nature of φ through external electric field adjustments within the proposed PS-DC-PCF PBS setup.

Since cores A and B of the PS-DC-PCF PBS are entirely symmetrical, and the distribution of the dielectric material is also identical, the propagating modes can be regarded as super-modes formed by the combination of four even and odd modes on the x-polarization (x-pol) and y-polarization (y-pol) directions. According to mode coupling theory, the propagation constants of the even and odd modes are different. As the x-pol and y-pol light propagates along the PS-DC-PCF PBS, it periodically transfers between the two cores. The propagation length required for the complete transfer of polarization light energy from one core to another is termed as the coupling length (CL). It is used to describe the distance required for x-pol light or y-pol light to be fully transmitted from one core to another. The calculation formula is as follows [25–27].

$$\mathrm{CL}_x = \frac{\lambda}{2(n_x^{\mathrm{even}} - n_x^{\mathrm{odd}})}, \tag{5}$$

$$\mathrm{CL}_\mathrm{y} = \frac{\lambda}{2(n_y^{\mathrm{even}} - n_y^{\mathrm{odd}})}, \tag{6}$$

where $\mathrm{CL_x}$ and $\mathrm{CL_y}$ represent the CLs of the x-pol and y-pol lights, respectively. n_x^{even}, n_x^{odd}, n_y^{even}, and n_y^{odd} refer to the effective refractive indices of the x-pol and y-pol even and odd modes, respectively. To achieve complete separation of the x-polarized and y-polarized lights, the length L of the PS-DC-PCF PBS must satisfy $\mathrm{L = mCL_x = nCL_y}$, and the CLR is defined as [28]

$$\mathrm{CLR} = \frac{\mathrm{CL_y}}{\mathrm{CL}_x}. \tag{7}$$

when CLR is equal to 0.5 or 2 [29], the splitting length of the PS-DC-PCF PBS can be expressed by $\mathrm{CL_x}$ or $\mathrm{CL_y}$. The device length is shorter in this case.

Assuming only the input port is fiber core A and excluding any consideration of transmission-induced attenuation of optical wave energy, the normalized powers of x-pol and y-pol at the output ports of fiber cores A and B are as follows [30]:

$$P_{\mathrm{out,A}}^{X,Y} = P_{\mathrm{in}} \cos^2\left(\frac{\pi}{2}\frac{L}{\mathrm{CL}_{x,y}}\right), \tag{8}$$

$$P_{\mathrm{out,B}}^{X,Y} = P_{\mathrm{in}} \sin^2\left(\frac{\pi}{2}\frac{L}{\mathrm{CL}_{x,y}}\right), \tag{9}$$

where L denotes the splitting length, while P_{in} and P_{out} refer to the incident light power and the output light powers of the two cores, respectively. Equations (8) and (9) facilitate the determination of the change in the NOP concerning the splitting length at a specified

wavelength, as well as the variation of the NOP concerning the wavelength at a given splitting length. Additionally, the extinction ratio (ER) is defined as [31]

$$\mathrm{ER} = 10\lg\frac{P_{\mathrm{out}}^{X}}{P_{\mathrm{out}}^{Y}}. \tag{10}$$

The performance assessment of the proposed PS-DC-PCF PBS can be conducted directly through the ER. An ER value exceeding 20 dB (or less than −20 dB) indicates that the power of one polarized light is 100 times greater than the other. This significant power discrepancy effectively facilitates the separation of the two orthogonally polarized beams [32]. Consequently, the wavelength range characterized by an ER exceeding 20 dB (or less than −20 dB) can be deemed as the operational bandwidth of the PS-DC-PCF PBS [33]. This criterion ensures efficient beam separation within the specified wavelength range.

The insertion loss (IL) is one of the key parameters used to evaluate the performance of PS-DC-PCF polarization beam splitters. It indicates the optical power loss suffered by the light signal after passing through the PBS, typically expressed in decibels (dB). Lower insertion loss implies higher optical signal transmission efficiency and better system performance. In optical communication systems, reducing insertion loss is crucial for ensuring the stability and reliability of signal transmission. Its calculation method is as follows [34]:

$$\mathrm{IL}_{x,y} = -10\lg\frac{P_{\mathrm{out},A}}{P_{\mathrm{in}}}. \tag{11}$$

3. Simulation Results and Discussion

The coupling and transmission characteristics of PS-DC-PCF were investigated using the FV-FEM. In the simulations, the incident light source was assumed to be a Gaussian beam, with the initial angle φ of the NLC (E7) molecules set to 90°, and the DC-PCF was assumed to operate at a temperature of 25 °C. The initial structural parameters were set to d_1 = 0.9 µm, d_2 = 1.2 µm, d_3 = 2.4 µm, d_4 = 1.3 µm, d_5 = 1.4 µm, and Λ = 2 µm, and the relationship between the effective refractive index of the even and odd super-modes for both x-pol and y-pol and the wavelength is shown in Figure 2.

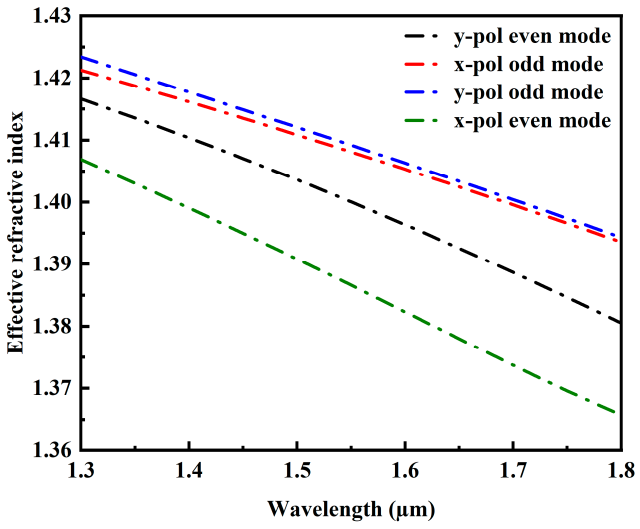

Figure 2. Effective refractive indices of the x-pol and y-pol odd and even super-modes of the designed PS-DC-PCF PBS.

As depicted in Figure 2, an evident trend emerges wherein the effective refractive indices of both x-polarized and y-polarized odd and even super-modes decrease with the augmentation of wavelength. Notably, a close proximity in the effective refractive indices of x-pol and y-pol odd super-modes is observed, contrasting with a discernible difference

in the effective refractive indices of x-pol and y-pol even super-modes. This discrepancy underscores the substantial impact of including NLC (E7) material on the effective refractive indices of x-pol and y-pol even super-modes, rendering them more predisposed to differentiation. Furthermore, Figure 2a highlights a progressive amplification in the disparity of effective refractive indices between x-pol and y-pol odd and even super-modes with increasing wavelength. Specifically, the divergence between x-polarized odd and even super-modes exceeds that between y-polarized odd and even super-modes, as evidenced by the graphical representation.

Figure 3 illustrates the relationship between the coupling lengths CL_x, CL_y, and CLR of the x-pol and y-pol odd and even super-modes with respect to wavelength, which can be calculated using Equations (5)–(7), respectively. From Figure 3, it can be observed that as the wavelength increases, CL_x is always smaller than CL_y. CL_x decreases gradually from 45.09 μm to 32.30 μm, while CL_y initially slightly increases from 95.76 μm to 96.47 μm and then significantly decreases to 65.19 μm. Considering the changing trends of CL_x and CL_y, the CLR curve initially increases and then decreases. However, within the considered wavelength range of 1.3–1.8 μm, the CLR value remains greater than 2. Under these conditions, although the x-pol light and y-pol light can be separated, the splitting length is too long.

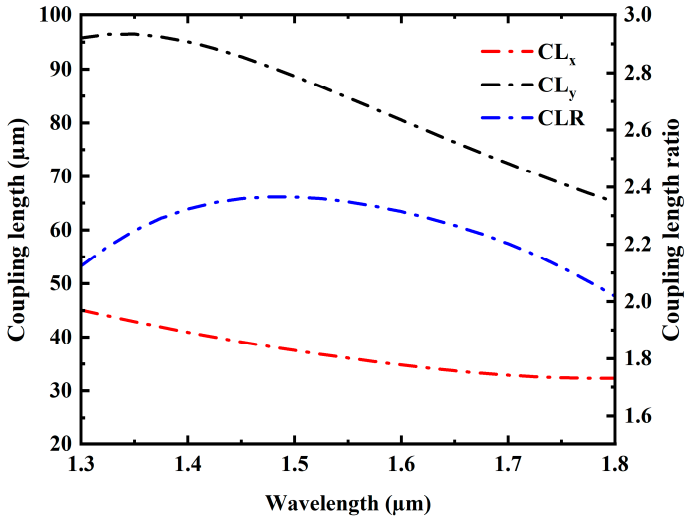

Figure 3. Variation of CL_x, CL_y, and CLR of the designed PS-DC-PCF PBS with wavelength.

Figure 4a–d illustrate the distributions of mode fields for four distinct super-modes within the PS-DC-PCF PBS, considering an incident light wavelength of 1.55 μm. Analyzing Figure 4a,b, it becomes apparent that the mode field energy associated with the x-pol and y-pol odd modes primarily resides within the fiber cores A and B, with only a minor portion extending into the central NLC aperture. Upon a closer examination of Figure 4c,d), it becomes evident that a fraction of energy from both the x-pol and y-pol even modes couples into the central aperture filled with an NLC. However, the mode field energy of these modes does not entirely confine within cores A and B, with a noteworthy observation being the dominance of energy from the x-pol even mode within the NLC aperture compared to the y-pol even mode. This finding accentuates the notable influence of the NLC filling on polarization even modes, particularly emphasizing its impact on the x-pol even mode.

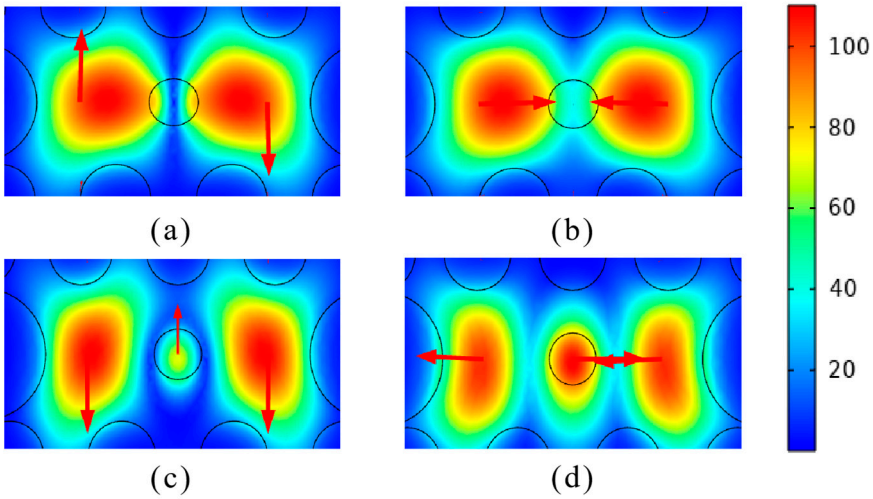

Figure 4. The mode field distributions of the (**a**) y-pol odd mode, (**b**) x-pol odd mode, (**c**) y-pol even mode, and (**d**) x-pol even mode in the designed PS-DC-PCF PBS.

To achieve a PS-DC-PCF PBS with optimal performance, the relationship between the structural parameters (d_1, d_2, d_3, d_4, and Λ) of the PS-DC-PCF PBS at a wavelength of 1.55 µm and CL_x, CL_y, and CLR was computed. The influence of d_1 on the CL_x, CL_y, and CLR of the PS-DC-PCF PBS is illustrated in Figure 5. From Figure 5, it can be observed that as d_1 increases from 0.6 to 1.0 µm, CL_x gradually increases from 33.67 µm to 36.55 µm, while CL_y increases to a maximum value of 85.89 µm from 63.55 µm and then gradually decreases to 75.07 µm. This is because the increase in d_1 enhances the influence of an NLC on mode coupling, thereby reducing the coupling strength in the x-pol direction and initially decreasing before increasing in the y-pol direction. Additionally, since the variation of CL_y is more pronounced than that of CL_x, the trend of CLR follows a similar pattern to that of CL_y. Furthermore, as d_1 increases, ε first increases from 1.89 to 2.41 and then decreases to 2.05.

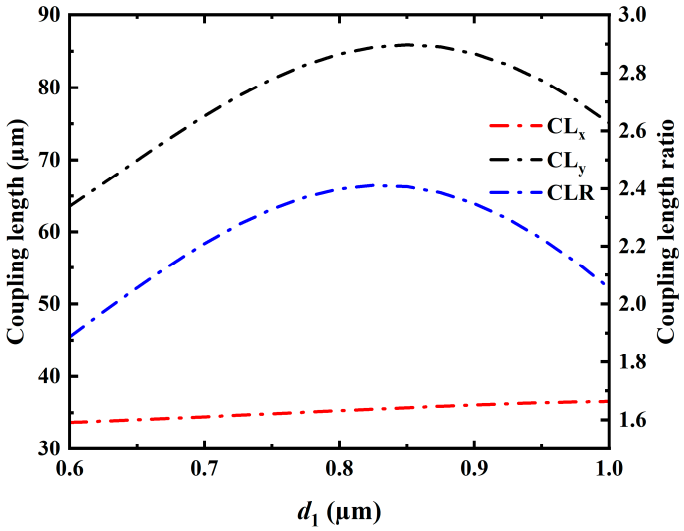

Figure 5. Effects of d_1 on the CL_x, CL_y and CLR of the PS-DC-PCF PBS at wavelength 1.55 µm when d_2 = 1.2 µm, d_3 = 2.4 µm, d_4 = 1.3 µm, d_5 = 1.4 µm and Λ = 2 µm.

The influence of d_2 on CL_x, CL_y, and CLR of the PS-DC-PCF PBS is depicted in Figure 6. From Figure 6, it can be observed that as d_2 increases from 1.1 µm to 1.5 µm, CL_x slightly decreases from 38.34 µm to 34.26 µm. In contrast, CL_y initially decreases significantly from 89.94 µm to 74.90 µm. With the increase in d_2, CLR first slightly increases from

2.35 to 2.37 and then decreases to 2.19. This indicates that the increase in d_2 weakens the confinement ability of the two cores for x-polarized odd and even super-modes, particularly for y-polarized odd and even super-modes, making the transmission between the two cores for x-pol and y-pol light easier.

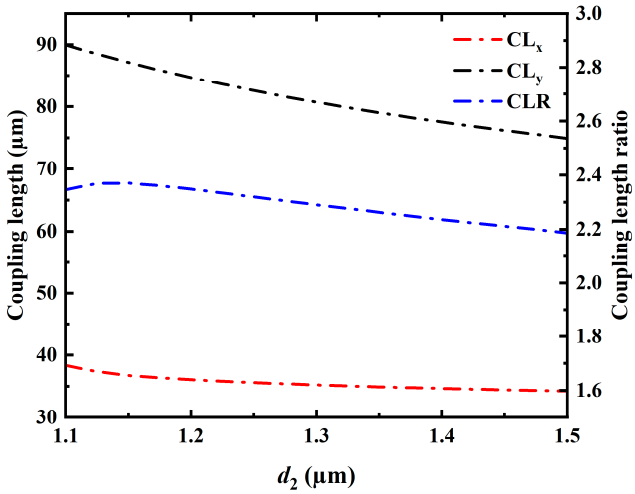

Figure 6. Effects of d_2 on the CL_x, CL_y and CLR of the PS-DC-PCF PBS at wavelength 1.55 μm when d_1 = 0.9 μm, d_3 = 2.4 μm, d_4 = 1.3 μm, d_5 = 1.4 μm and Λ = 2 μm.

Figure 7 illustrates the influence of d_3 on CL_x, CL_y, and CLR of the PS-DC-PCF PBS. From Figure 7, it can be observed that as d_3 increases from 2.0 μm to 2.6 μm, CL_x decreases from 42.31 μm to 33.78 μm, and CL_y decreases from 103.47 μm to 76.40 μm. Additionally, CLR also gradually decreases from 2.45 to 2.26 with the increase in wavelength. The main reason is that as d_3 increases, the coupling strength of x-pol and y-pol light increases, thus reducing the coupling length required for x-pol and y-pol light to propagate from one core to the other.

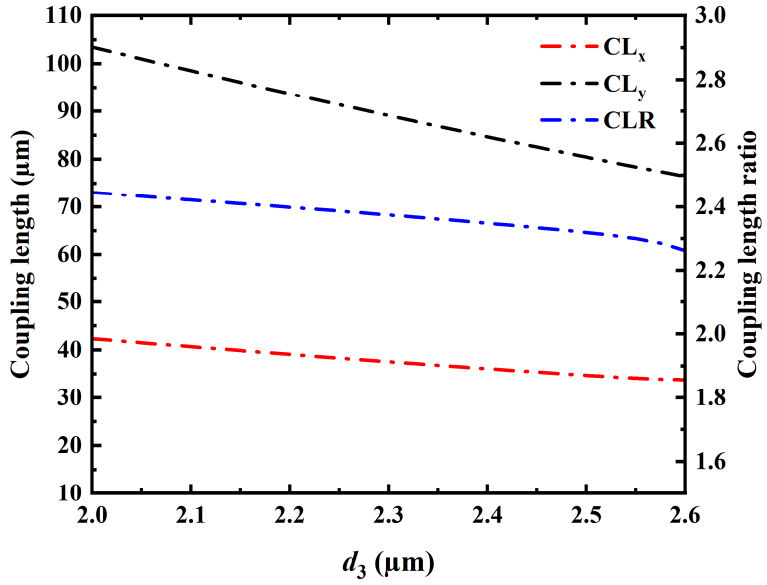

Figure 7. Effects of d_3 on the CL_x, CL_y and CLR of the PS-DC-PCF PBS at wavelength 1.55 μm when d_1 = 0.9 μm, d_2 = 1.2 μm, d_4 = 1.3 μm, d_5 = 1.4 μm and Λ = 2 μm.

Figure 8 demonstrates the impact of d_4 on CL_x, CL_y, and CLR of the PS-DC-PCF PBS. As shown in Figure 8, with the increase in d_4 from 1.2 μm to 1.6 μm, CL_x remains approximately at 36.1 μm and CL_y is essentially constant at about 84.7 μm, both exhibiting

only minimal variations. This indicates that changes in d_4 have almost no effect on the mode coupling between the two cores. Consequently, CLR consistently remains around 2.34 as d_4 increases.

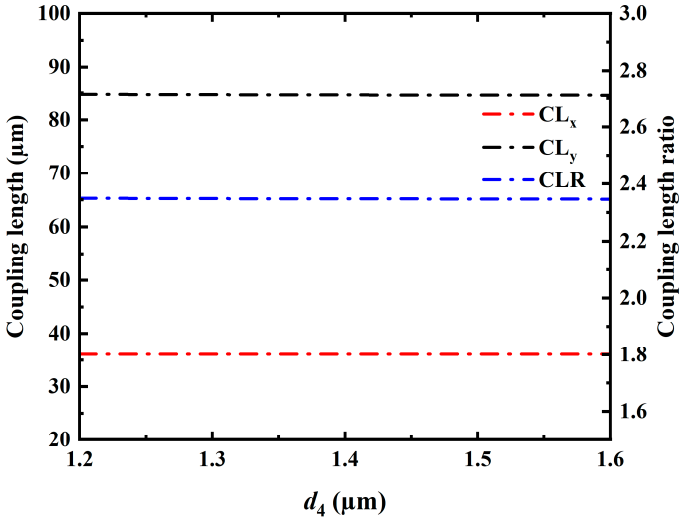

Figure 8. Effects of d_4 on the CL_x, CL_y and CLR of the PS-DC-PCF PBS at wavelength 1.55 μm when d_1 = 0.9 μm, d_2 = 1.2 μm, d_3 = 2.4 μm, d_5 = 1.4 μm and Λ = 2 μm.

Figure 9 depicts the influence of d_5 on CL_x, CL_y, and CLR of the PS-DC-PCF PBS. As d_5 increases from 1.3 μm to 1.7 μm, CL_x experiences a slight decrease from 36.56 μm to 35.72 μm, while CL_y decreases slightly more than CL_x, from 85.07 μm to 83.94 μm. CLR remains essentially constant at around 2.3, with minimal variations observed. This suggests that the variation in d_5 has a negligible impact on the mode coupling between the two cores.

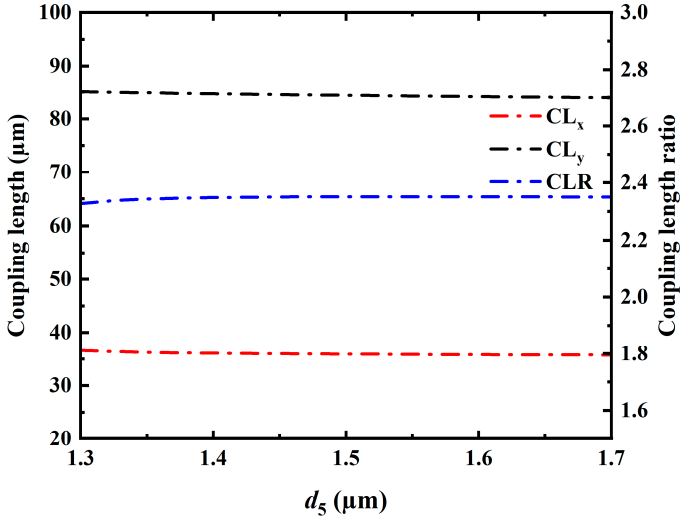

Figure 9. Effects of d_5 on the CL_x, CL_y and CLR of the PS-DC-PCF PBS at wavelength 1.55 μm when d_1 = 0.9 μm, d_2 = 1.2 μm, d_3 = 2.4 μm, d_4 = 1.3 μm and Λ = 2 μm.

Figure 10 illustrates the impact of Λ on CL_x, CL_y, and CLR of the PS-DC-PCF PBS. From Figure 10, it can be observed that as Λ increases from 1.85 μm to 2.1 μm, CLx gradually increases from 27.53 μm to 42.57 μm, and CL_y increases from 57.64 μm to 108.18 μm. The primary reason for this is that with the increase in pitch, the distance between core A and core B increases, leading to a weaker coupling strength between x-polarized and y-polarized light and thus an increase in coupling length. Additionally, since the increase

in CL_y is always greater than the increase in CL_x, CLR also increases with the increase in Λ, rising from 2.09 to 2.54.

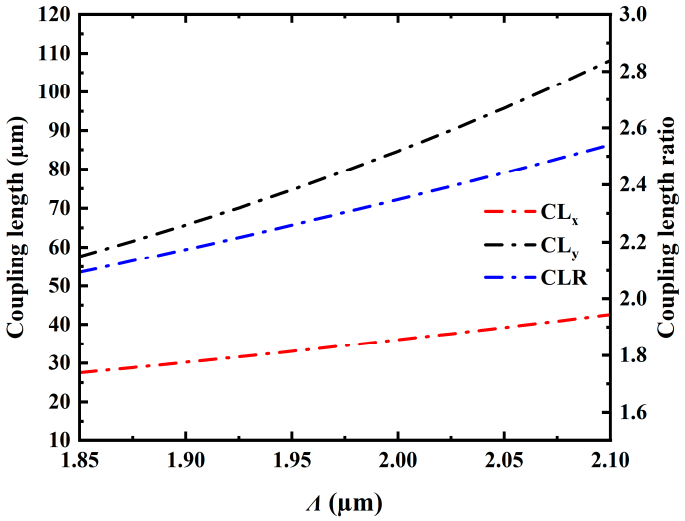

Figure 10. Effects of Λ on the CL_x, CL_y and CLR of the PS-DC-PCF PBS at wavelength 1.55 μm when d_1 = 0.9 μm, d_2 = 1.2 μm, d_3 = 2.4 μm, d_4 = 1.3 μm and d_5 = 1.4 μm.

By comparing the observations from Figures 5–10, we can notice that variations in each structural parameter influence the trends of CL_x, CL_y, and CLR. Particularly, when adjusting the parameters d_1 and Λ, the changes in CLR are relatively significant, with a span of approximately 0.5. This is because d_1 represents the aperture size of the central pore in the NLC, while Λ corresponds to the periodic structure of the photonic crystal. The periodic structure of the photonic crystal plays a crucial role in optical systems, determining the propagation of light within the crystal and the formation of photonic bandgaps. Therefore, fine-tuning these parameters directly affects the optical performance. In addition to the periodic structure of the photonic crystal, the NLC also plays a crucial role. The NLC possesses controllable birefringence characteristics, enabling precise control of light transmission behavior in optical devices. Hence, the role of the NLC cannot be overlooked in such structures. It complements the periodic structure of the photonic crystal, collectively influencing the ultimate optical performance.

After a thorough analysis of the impacts of structural parameters on CL_x, CL_y, and CLR, and by considering both the operational efficiency and fabrication intricacies associated with the PS-DC-PCF PBS, optimal structural parameters were identified: d_1 = 0.98 μm, d_2 = 1.4 μm, d_3 = 2.55 μm, d_4 = 1.3 μm, d_5 = 1.5 μm, and Λ = 2.0 μm. These refined parameters are deemed conducive to achieving desired performance characteristics while minimizing fabrication complexities.

Figure 11 illustrates the relationship between the optimized CL_x, CL_y, and CLR with wavelength in the presence and absence of an NLC filling in the central hole. From Figure 11a, it can be observed that when the PCF central hole is not filled with the NLC, i.e., when the central hole is an air hole, CL_x and CL_y are large, showing a decreasing trend within the wavelength range of 1.3–1.8 μm. CL_x decreases rapidly from 278.20 μm to 127.25 μm, and CL_y decreases from 357.85 μm to 161.60 μm, indicating a significant change. However, the change in CLR at this point is not very noticeable, showing an overall decreasing trend as the wavelength increases, from 1.286 to 1.270, almost staying between 1.27 and 1.29, far from the optimal value of 2 for CLR, which is not conducive to manufacturing shorter PBS. In contrast, from Figure 11b, it is evident that after filling the PCF central hole with the NLC, CL_x and CL_y decrease significantly and exhibit a more stable change. As the wavelength increases from 1.3 μm to 1.8 μm, CL_x gradually decreases from 39.59 μm to 27.48 μm, while CL_y initially increases from 56.59 μm to a maximum of 65.65 μm at a wavelength of 1.475 μm, then decreases to 55.83 μm. Comparing

these two scenarios, without an NLC filling in the central hole, there is a large variation in CL_x and CL_y, which may lead to an unstable propagation path of light in PCF, thus not conducive to polarization separation. However, after filling with the NLC, the infiltration of the NLC enhances the birefringence effect of PCF, greatly increasing the coupling intensity of x-pol and y-pol polarized light and making the light propagation path in PCF more controlled, which is beneficial for polarization separation, thereby achieving a shorter PBS splitter length and improving PBS performance. Additionally, as the wavelength increases, CLR shows an increasing then stabilizing trend. After calculation, it is found that CLR is closer to 2 at a wavelength of 1.625 μm, indicating that the optimized PS-DC-PCF PBS can achieve a shorter splitter length at this wavelength.

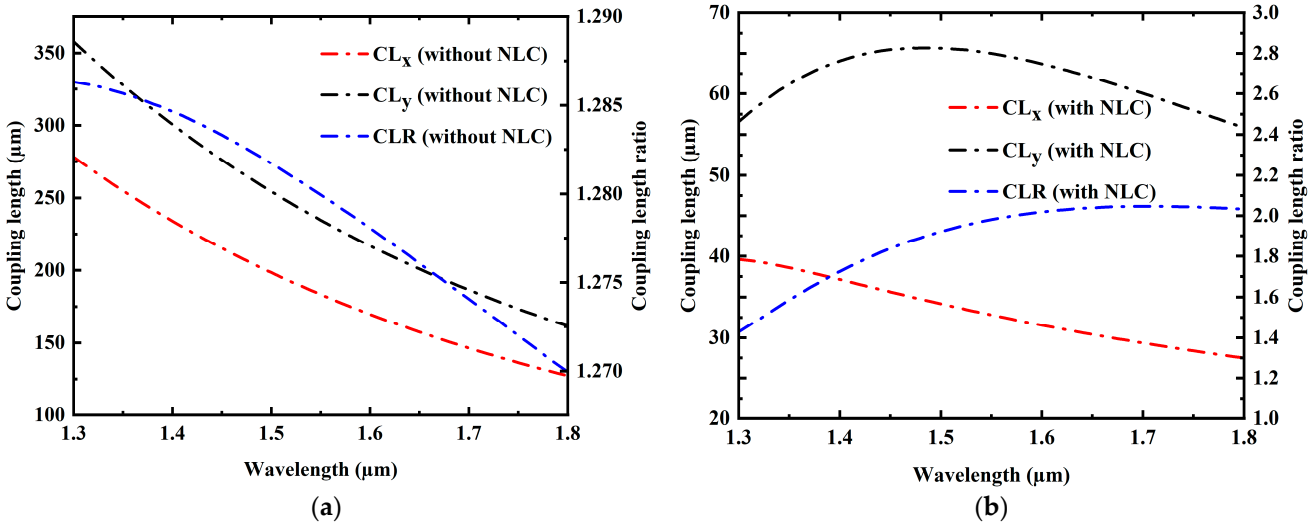

Figure 11. Variation of CL_x, CL_y, and CLR with wavelength at optimized structures (**a**) without NLC (**b**) with NLC.

According to Equations (8) and (9), the normalized output power (NOP) of x-pol and y-pol light in cores A and B will undergo periodic changes along the propagation distance. Figure 12a,b illustrate the relationship between NOP of x-polarized and y-polarized light at a wavelength of 1.625 μm and the propagation length. As shown in Figure 12a,b, as the propagation length increases from 0 to 61.9 μm, the NOP of x-polarized light completely transfers from core A to B and then returns to core A, reaching a maximum value of 1. Therefore, the shortest splitting length is 61.9 μm. At this length, the NOP of x-polarized light in core A reaches its minimum value, while that of y-polarized light reaches its maximum value. Conversely, in core B, the NOP of x-polarized light reaches its maximum value, while that of y-polarized light reaches its minimum value. Thus, when the splitting length is 61.9 μm, x-pol and y-pol light at a wavelength of 1.625 μm are completely separated in the two cores.

Figure 13 depicts the ER as a function of wavelength when the splitting length of the proposed PS-DC-PCF PBS is 61.9 μm. From Figure 13, it can be observed that as the wavelength increases from 1.3 μm to 1.325 μm, ER increases from 14.43 dB to 20.35 dB. As the wavelength continues to increase, ER reaches its first peak at 72.94 dB at a wavelength of 1.36 μm, and its second peak at 52.51 dB at a wavelength of 1.65 μm. At a wavelength of 1.75 μm, ER decreases to 20 dB. Therefore, within the wavelength range of 1.325 to 1.75 μm, ER stays above 20 dB, with a bandwidth of 423 nm, covering most of the communication bands (including O + E + S + C + L + U).

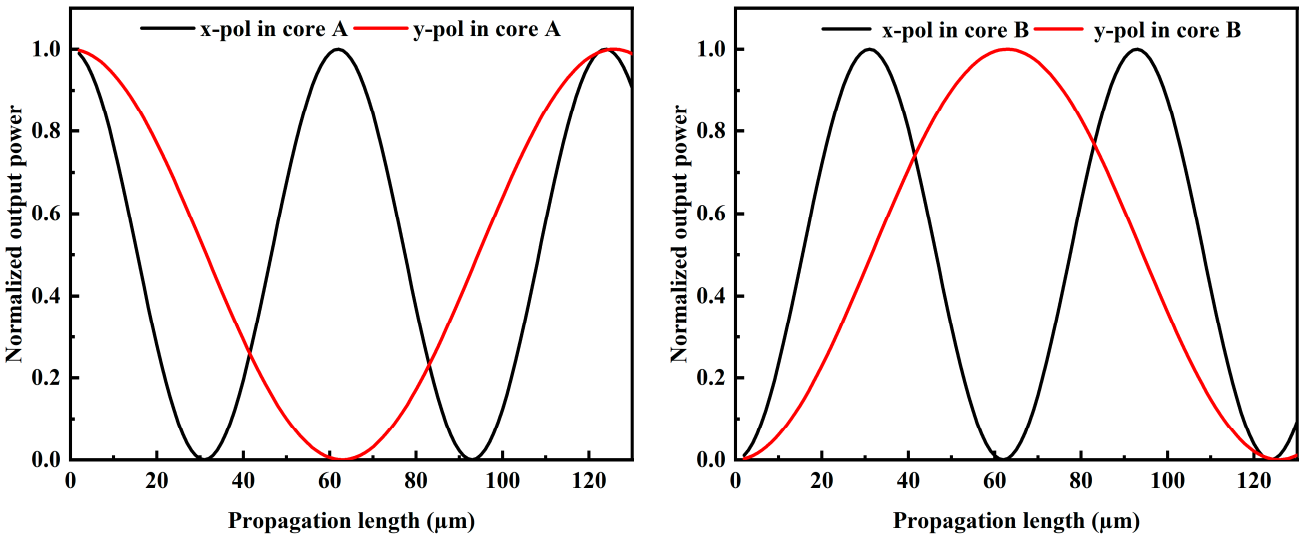

(**a**) (**b**)

Figure 12. NOPs of x-pol light and y-pol light in (**a**) core A and (**b**) core B of the PS-DC-PCF PBS with 1.625 μm incident light waves.

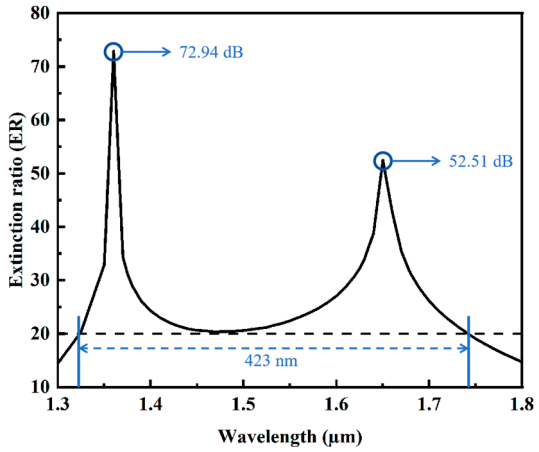

Figure 13. ER variation with wavelength in the PS-DC-PCF PBS for 61.9 μm splitting length.

In order to comprehensively characterize the spectral properties of the PS-DC-PCF PBS, Figure 14 depicts the insertion losses (IL_x and IL_y) as a function of wavelength. An examination of Figure 14 reveals distinct behaviors in IL_x and IL_y over the considered wavelength range. IL_x demonstrates a discernible decreasing trend until reaching a wavelength of 1.625 μm. Notably, IL_x experiences a rapid reduction from 2.23 dB, attaining a nadir of 8.99×10^{-6} dB at 1.625 μm, followed by a gradual increase to 0.70 dB at 1.8 μm. Conversely, IL_y exhibits comparably minor variations. Within the wavelength range of 1.3 to 1.36 μm, IL_y showcases a descending trajectory, plummeting from 0.10 dB to 1.50×10^{-7} dB. Subsequently, in the range of 1.36 to 1.47 μm, IL_y gradually ascends to 0.04 dB before declining anew within the 1.47 to 1.65 μm wavelength range, bottoming out at 2.43 × 10–5 dB at 1.65 μm, and eventually ascending to 0.13 dB within the 1.65 to 1.8 μm wavelength range. These observations underline the wavelength-dependent characteristics of IL_x and IL_y, thus highlighting the nuanced behavior of the PS-DC-PCF PBS across the specified spectral range.

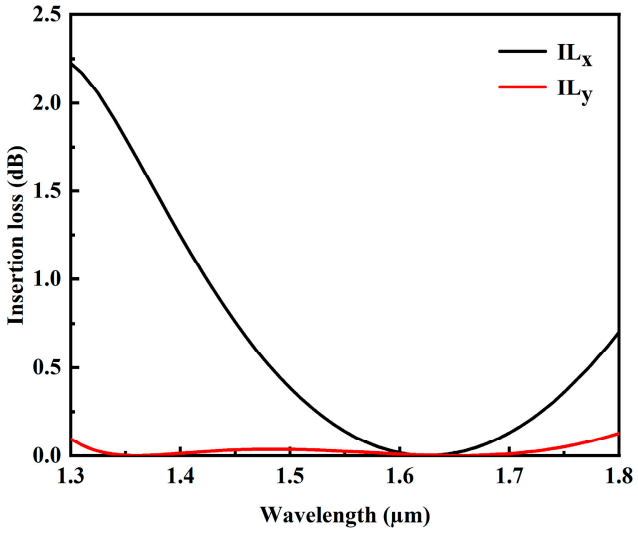

Figure 14. IL variation for x-pol and y-pol light across the 1.3 μm to 1.8 μm wavelength range.

To ensure the practical applicability of the designed PS-DC-PCF PBS, it is crucial to investigate the manufacturing tolerances of various structural parameters. Current manufacturing technologies can control errors within 1%, allowing for a precise evaluation of parameter variations. In this study, the impact of ±1% changes in different structural parameters on ER is analyzed. From the results illustrated in Figure 15a–f, it is apparent that the most significant influences on ER come from changes in the diameter of the central NLC-filled air holes (d_1) and the diameter of the adjacent air holes in the x-direction (d_3). According to Figure 15a, a 1% decrease in d_1 results in a wavelength range of 1.31 to 1.71 μm with ER exceeding 20 dB, yielding an effective working bandwidth of approximately 400 nm. Conversely, a 1% increase in d_1 expands the wavelength range with ER over 20 dB to 1.34~1.75 μm, widening the bandwidth to about 410 nm. This indicates that a reduction in d1 leads to a blue shift, while an increase leads to a red shift. Similarly, Figure 15c shows that a 1% decrease in d_3 yields an ER bandwidth of 1.32~1.74 μm (420 nm), while a 1% increase leads to a bandwidth of 1.33~1.73 μm (410 nm). The analysis also reveals that within the 1.34 to 1.71 μm wavelength range, ER remains consistently above 20 dB, regardless of variations in d_1, d_2, d_3, or Λ. Figure 15d,e show that 1% changes in d_4 and d_5 do not impact the operating bandwidth, with only minor variations in peak ER. In summary, even with a ±1% error margin during manufacturing, the designed PS-DC-PCF PBS maintains robust splitting performance across a broad bandwidth.

Due to the temperature-dependent refractive index of the NLC (E7), the relationship between ER and wavelength of the proposed PS-DC-PCF PBS at different temperatures is illustrated in Figure 16. It can be observed from Figure 16 that as the temperature varies from 15 °C to 35 °C, ER remains greater than 20 dB within the wavelength range of 1.37 μm to 1.68 μm. Additionally, with an increase in temperature from 15 °C to 35 °C, the operating bandwidth of the PS-DC-PCF PBS shifts towards shorter wavelengths, indicating a blue shift phenomenon. At 15 °C, the operating bandwidth is 400 nm, covering a wavelength range of 1.37 to 1.77 μm. Similarly, at 35 °C, the operating bandwidth is also approximately 400 nm, covering a wavelength range of 1.28 to 1.68 μm. These results demonstrate that the proposed PS-DC-PCF PBS can operate normally within the temperature range of 15 to 35 °C.

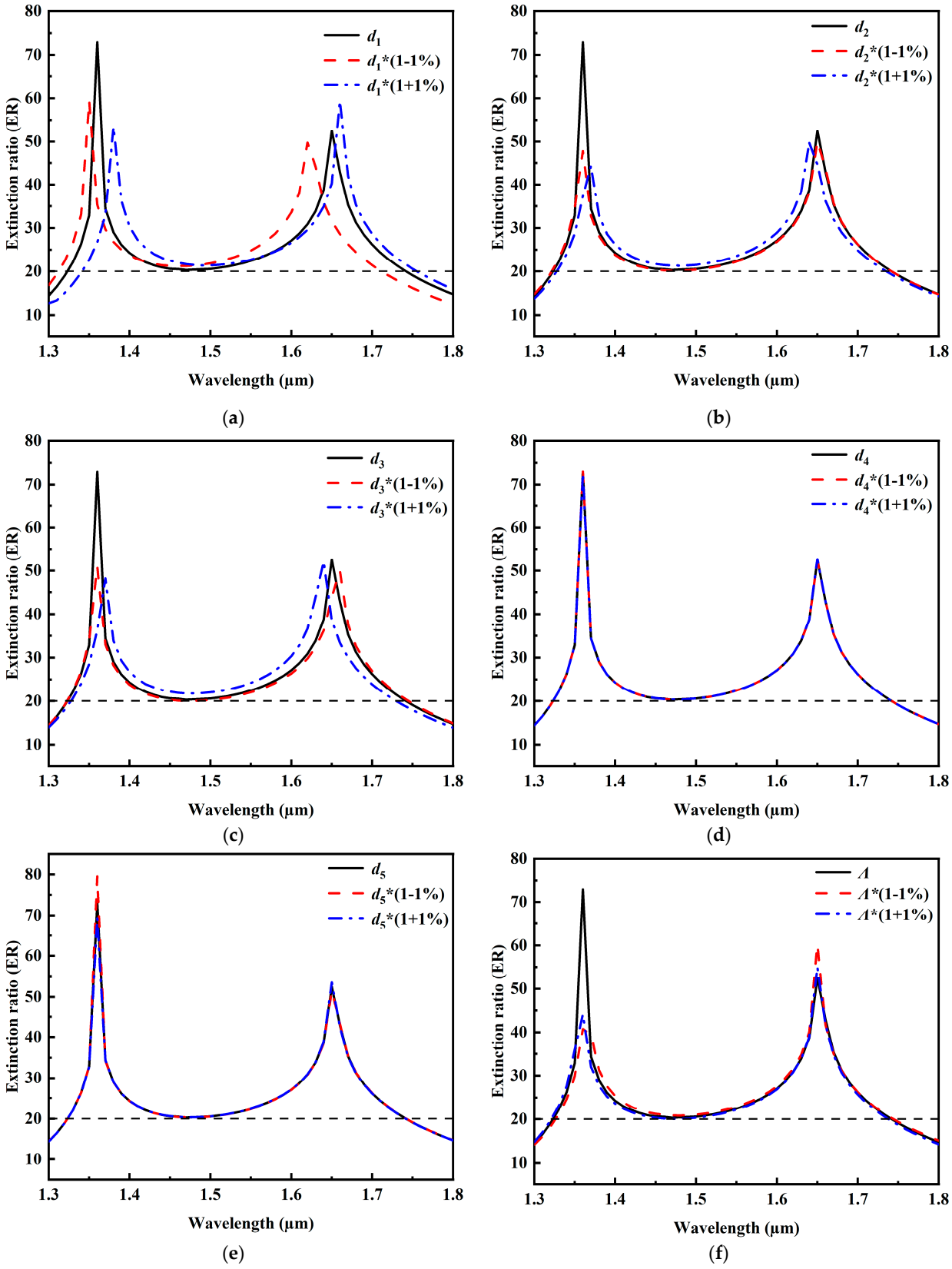

Figure 15. ER variation with a manufacturing tolerance of ±1% for structural parameter (**a**) d_1, (**b**) d_2, (**c**) d_3, (**d**) d_4, (**e**) d_5 and (**f**) Λ.

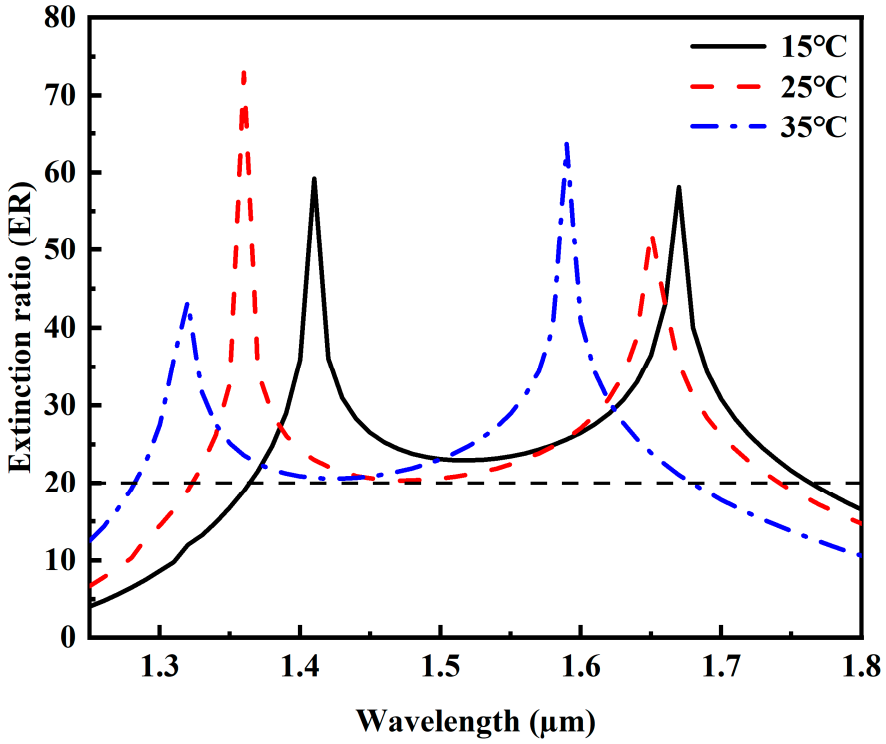

Figure 16. The effect of temperature on the ER.

Table 2 presents a comparison of the simulation results between the proposed PS-DC-PCF PBS and other reported DC-PCF PBSs. By observing Table 2, it is noted that the maximum ER values in references [12,14,35–37] are all higher than those within this study. However, it is worth noting that the operational bandwidth of PCF PBS refers to the wavelength range where ER is greater than 20 dB, while in some studies, the operational bandwidth may only exceed 10 dB [12,38] or 15 dB [36]. Therefore, even if the maximum ER value at a certain wavelength is high, the final spectral bandwidth may not necessarily be the widest. Hence, the crucial aspect lies in comparing the lengths of the splitters and the widths of the operational bandwidth. A further examination of the results in Table 2 reveals that most DC-PDF PBSs [13,35–41] neither possess the operational bandwidth proposed in this paper nor do they have shorter splitter lengths than the one in this study. It is important to note that the DC-PCF PBS structures proposed in references [35,36,38,41] include elliptical holes, indicating an increase in manufacturing complexity. Moreover, reference [41] employs a gold wire in their DC-PCF PBS structures, while this study utilizes an NLC, which is significantly cheaper than gold. Furthermore, this study does not include elliptical holes but adopts only circular holes, thus reducing manufacturing costs and structural manufacturing complexity. Additionally, it is noteworthy that references [12–14,37] also introduce an NLC to enhance the birefringence of PCF. Although the splitter lengths in references [12,14] are slightly shorter than those in this study, the operational bandwidth of this study exceeds theirs. In summary, the PS-DC-PCF PBS proposed in this study can simultaneously achieve shorter splitter lengths and a wider operational bandwidth, with lower costs and simpler manufacturing processes.

Table 2. Comparisons between the proposed PS-DC-PCF PBS and other reported DC-PCF PBSs.

References	Splitting Length (μm)	Bandwidth (nm)	Working Wavelength (μm)	Maximum ER (dB)
[12]	13.3390	200 (>10 dB)	1.445–1.645	143.49
[13]	94	349 (>20 dB)	1.352–1.701	72.2
[14]	58	335 (>20 dB)	1.306–1.641	90
[35]	93.3	70 (>20 dB)	1.51–1.58	−79.3
[39]	2000	100 (>20 dB)	1.45–1.55	−52.5
[40]	5900	116 (>20 dB)	1.481–1.597	−31
[38]	83.9	32.1 (>10 dB)	1.535–1.567	44.05
[36]	78	44 (>15 dB)	1.522–1.566	87
[41]	62.5	110 (>20 dB)	1.5–1.61	71
[37]	125	339 (>20 dB)	1.493–1.832	91
This work	61.9	423 (>20 dB)	1.324–1.747	72.94

4. Conclusions

In summary, a novel PS-DC-PCF PBS featuring a central cavity filled with an NLC was meticulously designed. Utilizing the FV-FEM, the polarization and coupling characteristics of the PS-DC-PCF PBS were thoroughly examined, leading to the determination of optimal structural parameters. Diverging from previous symmetric designs, the proposed PS-DC-PCF PBS boasts an asymmetrical configuration. Through the optimization of structural parameters, it achieves remarkable performance metrics including a minimal splitting length of merely 61.9 μm and an expansive working bandwidth spanning 423 nm (1.324–1.747 μm). This bandwidth effectively covers a wide spectrum of communication bands, encompassing most of the O + E + S + C + L + U bands. Furthermore, the meticulously designed PS-DC-PCF PBS demonstrates robust manufacturing tolerances and resistance to interference. It is poised to play a pivotal role in providing essential device support for the advancement of future all-optical communication systems.

In general, the PS-DC-PCF PBS exhibits broad potential in both practical applications and future implications. It serves not only to separate and control the polarization state of light signals in optical communication systems but also finds utility in optical sensors, laser systems, and various optical devices. By splitting incident light signals into two polarization states, the PS-DC-PCF PBS enhances the performance and stability of optical communication systems, propels the advancement of optical sensor technology, fosters progress in laser technology, and fosters innovation in the field of optical devices. With the continuous advancement of optical technology and the increasing demands of applications, the PS-DC-PCF PBS is poised to become a significant component in the realm of optics, offering new possibilities and solutions across various application domains.

Author Contributions: Conceptualization, Y.J. and H.Z.; methodology, Y.J. and Y.D.; software, Y.J. and Y.D.; validation, Y.J., Y.D. and H.Z.; formal analysis, Y.J., Y.D. and J.D.; investigation, Y.J., Y.D., R.Z. and D.Z.; resources, Y.J.; data curation, Y.J.; writing—original draft preparation, Y.J.; writing—review and editing, Y.J., J.D. and H.Z.; visualization, Y.J. and Y.D.; supervision, Y.J. and Y.D.; project administration, Y.J., R.Z., D.Z. and H.Z.; funding acquisition, H.Z. All authors have read and agreed to the published version of the manuscript.

Funding: This work was supported by the National Natural Science Foundation of China under Grant No. 61405096. No. 61504058 and the introduction of talent research and Research Fund of Nanjing University of Posts and Telecommunications (NY214158), and the Open fund of Laboratory of Solid State Microstructures, Nanjing University (M28035), and the Open fund of State Key Laboratory of Transient Optics and Photonics, Chinese Academy of Sciences (SKLST201404). We would like to express our sincere thanks to the above organizations.

Data Availability Statement: Data underlying the results presented in this paper are not publicly available at this time but may be obtained from the authors upon reasonable request.

Conflicts of Interest: The authors declare no conflict of interest.

References

1. Knight, J.C.; Birks, T.A.; Russell, P.S.J.; Atkin, D.M. All-silica single-mode optical fiber with photonic crystal cladding: Errata. *Opt. Lett.* **1997**, *22*, 484–485. [CrossRef]
2. Zhang, J.-X. Dual-core PCF-based THz polarization beam splitter with broad bandwidth and ultra-high extinction ratio. *Optik* **2022**, *251*, 168425. [CrossRef]
3. Knight, J.C.; Birks, T.A.; Cregan, R.F.; Russell, P.S.J.; De Sandro, J.P. Large Mode Area Photonic Crystal Fiber. *Electron. Lett.* **1998**, *34*, 1347–1348. [CrossRef]
4. Dudley, J.M.; Genty, G.; Coen, S. Supercontinuum generation is photonic crystal fiber. *Rev. Mod. Phys.* **2006**, *78*, 1135–1184. [CrossRef]
5. Zhang, Y.; Wang, L.; Jia, P.; Zhai, C.; An, G.; Liu, L.; Zhu, F.; Su, J. High-sensitivity refractive index sensor with cascaded dual-core photonic crystal fiber based on vernier effect. *Optik* **2022**, *256*, 168488. [CrossRef]
6. Chen, N.; Ding, X.; Wang, L.; Xiao, Y.; Guo, W.; Huang, Y.; Guo, L.; Liu, C.; Xu, Y. Broadband Polarization Beam Splitter Based on Silicon Dual-Core Photonic Crystal Fiber with Gold Layers Operating in Mid-Infrared Band. *Plasmonics* **2023**. [CrossRef]
7. Al Mahfuz, M.; Hossain, A.; Haque, E.; Hai, N.H.; Namihira, Y.; Ahmed, F. Dual-Core Photonic Crystal Fiber-Based Plasmonic RI Sensor in the Visible to Near-IR Operating Band. *IEEE Sens. J.* **2020**, *20*, 7692–7700. [CrossRef]
8. Coelho, A.G.; Costa, M.B.C.; Ferreira, A.C.; da Silva, M.G.; Lyra, M.L.; Sombra, A.S.B. Realization of All-Optical Logic Gates in a Triangular Triple-Core Photonic Crystal Fiber. *J. Light. Technol.* **2013**, *31*, 731–739. [CrossRef]
9. Djob, R.B. Modulation instability in an asymmetric triple-core photonic crystal fiber with higher order dispersion and higher order nonlinear effects. *Far East J. Appl. Math.* **2021**, *110*, 1–18. [CrossRef]
10. Tang, Z.; Lou, S.; Wang, X.; Zhang, W.; Yan, S.; Xing, Z. Using Mode Coupling Mechanism in Symmetrical Triple-Core Photonic Crystal Fiber for High Performance Strain Sensing. *IEEE J. Sel. Top. Quantum Electron.* **2020**, *26*, 1–7. [CrossRef]
11. Younis, B.M.; Heikal, A.M.; Hameed, M.F.O.; Obayya, S.S.A. Highly wavelength-selective asymmetric dual-core liquid photonic crystal fiber polarization splitter. *J. Opt. Soc. Am. B* **2018**, *35*, 1020–1029. [CrossRef]
12. An, S.; Shi, Y.; Yi, Z.; Liu, C.; Sun, T.; Lv, J.; Yang, L.; Chu, P.K. Ultra-short dual-core GaAs photonic crystal fiber splitter filled with nematic liquid crystal. *Opt. Eng.* **2021**, *60*, 056104. [CrossRef]
13. Qu, Y.; Han, Y.; Yuan, J.; Zhou, X.; Yan, B.; Wang, K.; Sang, X.; Yu, C. A Novel Liquid Crystal-Filled, Dual-Core Photonic Crystal Fiber Polarization Beam Splitter Covering the E + S + C + L + U Communication Band. *Photonics* **2021**, *8*, 461. [CrossRef]
14. Xu, Y.; Yuan, J.; Qu, Y.; Qiu, S.; Zhou, X.; Yan, B.; Wang, K.; Sang, X.; Yu, C. Ultra-short polarization beam splitter based on rhombic structure dual-core photonic crystal fiber with a central hole filled nematic liquid crystal. *J. Opt. Soc. Am. B* **2023**, *40*, 206–214. [CrossRef]
15. Al Mahfuz, M.; Mollah, A.; Momota, M.R.; Paul, A.K.; Masud, A.; Akter, S.; Hasan, R. Highly sensitive photonic crystal fiber plasmonic biosensor: Design and analysis. *Opt. Mater.* **2019**, *90*, 315–321. [CrossRef]
16. Gamal, Y.; Younis, B.; Hegazy, S.; Badr, Y.; Hameed, M.F.O.; Obayya, S. Highly efficient modified dual D-shaped PCF polarization filter. *Opt. Fiber Technol.* **2021**, *62*, 102459. [CrossRef]
17. Wang, G.; Lu, Y.; Yang, X.; Duan, L.; Yao, J. High-sensitivity magnetic field sensor based on a dual-core photonic crystal fiber. *Appl. Opt.* **2019**, *58*, 5800–5806. [CrossRef] [PubMed]
18. Reyes-Vera, E.; Usuga-Restrepo, J.; Jimenez-Durango, C.; Montoya-Cardona, J.; Gomez-Cardona, N. Design of low-loss and highly birefringent Porous-Core Photonic Crystal Fiber and Its Application to Terahertz Polarization Beam Splitter. *IEEE Photonics J.* **2018**, *10*, 1–13. [CrossRef]
19. Born, M.; Wolf, E. Principles of Optics Electromagnetic Theory of Propagation, Interference and Diffraction of Light. *Phys. Today* **2000**, *53*, 77–78. [CrossRef]
20. Wang, E.-L.; Jiang, H.-M.; Xie, K.; Chen, C.; Hu, Z.-J. Polarization splitter based on dual core liquid crystal-filled holey fiber. *J. Appl. Phys.* **2016**, *120*, 114501. [CrossRef]
21. Chen, H.L.; Li, S.G.; Fan, Z.K.; An, G.W.; Li, J.S.; Han, Y. A novel polarization splitter based on dual-core photonic crystal fiber with a liquid crystal modulation core. *IEEE Photonics J.* **2014**, *6*, 1–9. [CrossRef]
22. Hameed, M.F.O.; Obayya, S.S.A. Coupling Characteristics of Dual Liquid Crystal Core Soft Glass Photonic Crystal Fiber. *IEEE J. Quantum Electron.* **2011**, *47*, 1283–1290. [CrossRef]
23. Wang, Y.; Shen, J.; Li, S. Surface plasmon induced broadband single-polarization filter based on high birefringence photonic crystal fiber. *Optik* **2020**, *206*, 164255. [CrossRef]
24. Hagras, E.A.; Hameed, M.F.O.; Heikal, A.; Obayya, S. Multi-functional photonic crystal fiber splitter for the two communication bands. *Opt. Fiber Technol.* **2019**, *52*, 101986. [CrossRef]
25. Anbazhagan, L.; Ganesan, G. Polarization-independent wavelength splitter based on silicon nanowire embedded dual-core pentagonal lattice photonic crystal fiber for optical communication systems. *Opt. Eng.* **2021**, *60*, 047103. [CrossRef]
26. Bai, Y.; Hao, R.; Yuan, B.; Cao, B. An ultrashort length and high extinction ratio polarization beam splitter based on dual-core PCF. *J. Opt.* **2021**, *50*, 257–263. [CrossRef]
27. Fan, Z.; Li, S.; Liu, Q.; Li, J.; Xie, Y. Plasmonic Polarization Beam Splitter Based on Dual-Core Photonic Crystal Fiber. *Plasmonics* **2015**, *10*, 1283–1289. [CrossRef]

28. Zou, H.; Xiong, H.; Zhang, Y.-S.; Ma, Y.; Zheng, J.-J. Ultra-broadband polarization splitter based on graphene layer-filled dual-core photonic crystal fiber. *Chin. Phys. B* **2017**, *26*, 124216. [CrossRef]
29. Zheng, G.M. Mid-infrared broadband polarization beam splitter based on GaS photonic crystal fiber with high extinction ratio. *Optik* **2021**, *241*, 166971. [CrossRef]
30. Rahman, T.; Khaleque, A. Ultra-short polarization splitter based on a plasmonic dual-core photonic crystal fiber with an ultra-broad bandwidth. *Appl. Opt.* **2019**, *58*, 9426–9433. [CrossRef]
31. Zhang, X.; Yuan, J.; Wang, K.; Kang, Z.; Yan, B.; Sang, X.; Wu, Q.; Yu, C.; Farrell, G. Strong Modulation Instability in a Silicon–Organic Hybrid Slot Waveguide. *IEEE Photon-J.* **2015**, *7*, 1–8. [CrossRef]
32. Khaleque, A.; Hattori, H.T. Ultra-broadband and compact polarization splitter based on gold filled dual-core photonic crystal fiber. *J. Appl. Phys.* **2015**, *118*, 143101. [CrossRef]
33. Zhao, T.; Lou, S.; Wang, X.; Zhou, M.; Lian, Z. Ultrabroadband polarization splitter based on three-core photonic crystal fiber with a modulation core. *Appl. Opt.* **2016**, *55*, 6428–6434. [CrossRef]
34. Dou, C.; Jing, X.; Li, S.; Wu, J.; Wang, Q. A compact and low-loss polarization splitter based on dual-core photonic crystal fiber. *Opt. Quantum Electron.* **2018**, *50*, 255. [CrossRef]
35. Revathi, A.A.; Rajeswari, D. Ultra-short polarization beam splitter based on dual core photonic crystal fiber. *J. Mod. Opt.* **2016**, *76*, 117.
36. Wang, J.; Pei, L.; Weng, S.; Wu, L.; Li, J.; Ning, T. Ultrashort polarization beam splitter based on liquid-filled dual-core photonic crystal fiber. *Appl. Opt.* **2018**, *57*, 3847. [CrossRef]
37. Xu, Y.; Yuan, J.; Li, Y.; Qu, Y.; Zhou, X.; Yan, B.; Wang, K.; Sang, X.; Yu, C. Design of an octagon structure dual-core photonic crystal fiber polarization beam splitter with a liquid crystal filled central hole. *Opt. Commun.* **2023**, *546*, 129765. [CrossRef]
38. Xu, Q.; Luo, W.; Li, K.; Copner, N.; Lin, S. Design of Polarization Splitter via Liquid and Ti Infiltrated Photonic Crystal Fiber. *Crystals* **2019**, *9*, 103. [CrossRef]
39. Rajeswari, D.; Raja, A.S.; Selvendran, S. Design and analysis of polarization splitter based on dual-core photonic crystal fiber. *Optik* **2017**, *144*, 15–21. [CrossRef]
40. Chen, M.-Y.; Sun, B.; Zhang, Y.-K.; Fu, X.-X. Design of broadband polarization splitter based on partial coupling in square-lattice photonic-crystal fiber. *Appl. Opt.* **2010**, *49*, 3042–3048. [CrossRef]
41. Wang, K.; Qu, Y.; Yuan, J.; Qiu, S.; Zhou, X.; Yan, B.; Wu, Q.; Liu, B.; Wang, K.; Sang, X.; et al. Ultra-short polarization beam splitter based on dual-core photonic crystal fiber with surface plasmon resonance effect. *Opt. Eng.* **2021**, *60*, 076104. [CrossRef]

Disclaimer/Publisher's Note: The statements, opinions and data contained in all publications are solely those of the individual author(s) and contributor(s) and not of MDPI and/or the editor(s). MDPI and/or the editor(s) disclaim responsibility for any injury to people or property resulting from any ideas, methods, instructions or products referred to in the content.